energies

Article

Research on Vibration Energy Recovery from a Horizontal Seat Suspension System

Igor Maciejewski *, Sebastian Pecolt, Andrzej Blazejewski, Bartosz Jereczek, Tomasz Krolikowski and Tomasz Krzyzynski

Department of Mechatronics and Automation, Faculty of Mechanical and Energy Engineering, Koszalin University of Technology, Sniadeckich 2, 75-453 Koszalin, Poland; sebastian.pecolt@tu.koszalin.pl (S.P.); andrzej.blazejewski@tu.koszalin.pl (A.B.); bartosz.jereczek@tu.koszalin.pl (B.J.); tomasz.krolikowski@tu.koszalin.pl (T.K.); tomasz.krzyzynski@tu.koszalin.pl (T.K.)

* Correspondence: igor.maciejewski@tu.koszalin.pl; Tel.: +48-94-3478-471

Abstract

This paper presents an experimental study of vibration energy recovery from a horizontal seat suspension system in which a brushless direct current (BLDC) motor is used as both an active force actuator and a controllable regenerative braking element. The novelty of the study lies in the experimental validation of an active/regenerative switching strategy for a horizontal seat suspension and in the quantitative comparison of passive, fully active and regenerative operating modes under random vibration excitation and different inertial loads. The proposed system was evaluated using transmissibility functions, seat effective amplitude transmissibility (SEAT) factors, suspension travel, and electrical quantities generated in the braking branch. The results show that the fully active mode provides the highest vibration attenuation, whereas the regenerative mode reduces the SEAT factor compared with the passive suspension while simultaneously producing measurable electrical power in the braking resistor network. The maximum measured electrical power in the braking branch reached 7.692 W for the WN3 excitation signal and an 80 kg load. The obtained results confirm the practical potential of regenerative braking for potentially reducing the net energy demand of active seat suspension systems, while also highlighting the trade-off between vibration attenuation, suspension travel, and recoverable electrical power.

Keywords: horizontal seat suspension system; vibration control; energy harvesting

1. Introduction

Energy harvesting from vibrating systems is a key research area in the fields of mechanical and electrical engineering. It is also important in materials technology. The phenomenon is based on the conversion of mechanical energy, generated by ambient or system vibrations, into useful electrical energy. This energy can be used to supply Internet of Things (IoT) sensors, autonomous low-power systems, or auxiliary devices, and it can also reduce the total external energy demand of vibration-control systems. The primary vibration energy recovery methods include electromagnetic, electrostatic, and piezoelectric solutions. These three technologies use a different energy conversion process, which determines their effectiveness, implementation limitations, and range of applications.

The piezoelectric conversion uses piezoelectric materials such as different types of ceramics [1,2], polymers [3,4], composites [5] or organic materials [6]. The phenomenon that allows for the accumulation of energy is called a piezoelectric effect and was first

Received: 25 June 2026
Revised: 13 July 2026
Accepted: 31 July 2026
Published: 2 August 2026

 https://doi.org/10.3390/en19153628

observed in 1880 by the Pierre and Jacques Curie brothers. The ions or charges in a material are asymmetrically shifted when mechanical stress occurs. Their small size and low weight are suitable for use in energy recovery subsystems in a wide range of ground transport, for example, roadways [7], rails [8], bridges [9], or speed bumps [10], and in areas related to everyday duties and natural phenomena.

Energy harvesters based on electrostatic conversion usually use the variable capacitance of capacitors. They convert vibrations from microelectromechanical systems into electrical energy when relative motion between two plates is present. The efficiency of this method depends on the scale of the system, and its highest values are found in very small-scale systems such as microsensors. The major use of them is for medical purposes like intra-cardiac implants [11], neural implants [12], or wearable devices [13].

Electromagnetic harvesters work in accordance with Faraday's Law. The energy is produced when magnetic flux induces a current in a coil or conductor. This method is commonly and widely used in automotive [14,15], railway [16], and other regenerative systems [17]. This method is characterized by long-lifetime work, robustness, and higher output currents than previously mentioned ones. There are also some disadvantages like low output voltage and lower efficiency at small sizes of electromagnetic devices [18]. There are various configurations of technical solutions in the aspect of structures like single or multiple [19] magnet usage or in the aspect of moving parts like harvesters with moving coils [20] or magnets [21].

A further evolution of electromagnetic harvesters can be considered as recuperative braking. In such systems, kinetic energy during braking phases of electric motors can produce portion of electrical energy in accordance with induction laws. It can be redirected to recharge batteries or supercapacitors, or can be used directly to power sensors present in the system, thereby contributing to the overall energy efficiency of the device. Moreover, advanced control strategies are employed to regulate the energy conversion process, ensuring optimal performance while minimizing potential issues like fluctuation in power output.

Regenerative and semi-active vibration-control systems are particularly relevant for seat and vehicle suspension applications because they involve a direct compromise between vibration attenuation, suspension travel and recoverable electrical energy. Recent studies have investigated electromagnetic dampers, semi-active suspension systems, and inerter-based concepts, including phase-deviation compensation in semi-active suspension control [22]. However, many of these studies focus on vertical vehicle suspension, electromagnetic damping or general energy harvesting, whereas fewer papers experimentally analyze a horizontal seat suspension in which the same electric motor operates both as an active actuator and as a regenerative braking element.

Recuperative braking can also be used for semi-active and active seat suspension systems. As mentioned in [23], the permanent magnet synchronous motor (PMSM) was adapted to the vehicle body and unsprung mass via mounting rings and played the role of electromagnetic damper. With an external circuit equipped with resistors and metal–oxide–semiconductor field-effect transistor (MOSFET) drivers, this solution provides the possibility for controlling the damping force of suspensions by connecting phases of the motor in various series-parallel resistor configurations, providing the possibility of semi-active control of the seat suspension system. In the present paper, this idea is extended so that the brushless direct current (BLDC) motor acts as a force generator opposing the seat suspension forces or as an energy harvester in regenerative braking mode, which will be explained further in the publication.

The main research gap addressed in this paper is the lack of experimental verification of the trade-off between vibration isolation performance and recoverable electrical power in a horizontal active seat suspension system operating under random excitation and different mass loads. The main contributions of this study are as follows: (I) development of a BLDC-motor-based horizontal seat suspension system operating in motoring and regenerative braking modes; (II) identification of the active and braking force characteristics required for control implementation; (III) experimental comparison of passive, fully active, and regenerative suspension modes under different excitation intensities and mass loads; and (IV) quantitative assessment of vibration isolation performance using transmissibility, SEAT factor, and suspension travel together with RMS current, average electrical power, and recoverable energy generated in the braking branch.

From a practical point of view, harvesting additional energy available from working devices is preferable to relying exclusively on external power sources because it can reduce the net energy demand of active systems. In the present prototype, the generated electrical energy is dissipated in a controlled resistor network; therefore, the reported electrical quantities should be interpreted as recoverable energy potential rather than net stored energy.

2. Physical and Mathematical Model of the Active Horizontal Seat Suspension

In Figure 1a a schematic representation of an active horizontal seat suspension system is presented. The seat is connected to the servo-drive, which provides active force F_{ax}, generated via control inputs u_{a}, u_{b}, u_{c} and, subsequently, the electrical currents i_{a}, i_{b}, i_{c}. The motor generates a torque T_{e} directly on the rotor of angular displacement θ_{e}, influencing the seat's horizontal vibration q_{x}. The mass m simulates the driver presence that is exposed to the input vibration q_{sx} considered as external disturbances. The Figure 1b shows an actual experimental set-up used to test the vibro-isolation properties of the seat. The seat is mounted on a test rig with mechanical components that simulate real-world vibrations and forces. The setup includes sensors and actuators to measure the seat's response to vibrations, ensuring that the active suspension system can effectively mitigate unwanted oscillations.

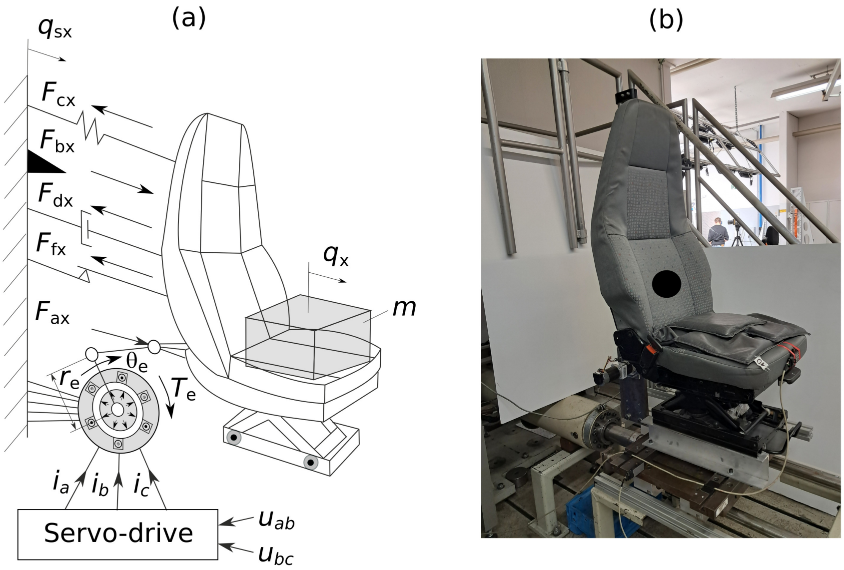

Figure 1. Physical model of the active horizontal seat suspension (**a**) and experimental set-up for measuring its vibro-isolation properties (**b**).

To measure the vibration of both the shaker and the suspended mass, two high-output linear accelerometers are utilized. Additionally, a cable extension position sensor tracks the relative displacement of the suspension mechanism. A PC-based data acquisition system,

https://doi.org/10.3390/en19153628

i.e., comprising modular hardware, application software, and a computer, is employed to capture and process these measurements. The equation of motion for an active horizontal seat suspension is defined as the sum of forces acting on the isolated body:

$$m\ddot{q}_{\mathrm{x}} = -F_{\mathrm{cx}} \pm F_{\mathrm{bx}} - F_{\mathrm{dx}} - F_{\mathrm{fx}} + F_{\mathrm{ax}} \tag{1}$$

where m is the mass of isolated body, q_{x} is the displacement of a seat, F_{cx} is the conservative force of two tension springs, F_{bx} is the discontinuous force of end-stop buffers that limit the overall stroke of a horizontal suspension, F_{dx} is the damping force of a shock-absorber, F_{fx} is the dissipative friction force of a suspension mechanism. The mathematical models of the passive forces mentioned above are discussed in the Authors' previous paper [24]. The electromagnetic torque T_{e} is generated by using the BLDC motor, which is, in turn, converted into the horizontal force F_{ax}. The resulting active force is defined as follows:

$$F_{\mathrm{ax}} = \frac{p\lambda}{r_{\mathrm{e}}}(\phi_{\mathrm{a}} i_{\mathrm{a}} + \phi_{\mathrm{b}} i_{\mathrm{b}} + \phi_{\mathrm{c}} i_{\mathrm{c}}) \tag{2}$$

where p is the number of pole pairs, λ is the amplitude of flux induced by permanent magnets, r_{e} is the length of a lever arm coupling the motor and suspension system, ϕ_{a}, ϕ_{b}, ϕ_{c} are the phase electromotive forces that are trapezoidal in the case of BLDC motors and i_{a}, i_{b}, i_{c} are the phase currents flowing through the motor windings. These currents are oriented in the three-phase reference frame (*abc*-frame) and are determined as follows [25]:

$$\begin{aligned}
\dot{i}_{\mathrm{a}} &= \frac{1}{3L_{\mathrm{s}}}\left[u_{\mathrm{ab}} + u_{\mathrm{bc}} - 3(R_{\mathrm{s}} - R_{\mathrm{ext}})i_{\mathrm{a}} + 3\lambda p\dot{\theta}_{\mathrm{r}}(-2\phi_{\mathrm{a}} + \phi_{\mathrm{b}} + \phi_{\mathrm{c}})\right] \\
\dot{i}_{\mathrm{b}} &= \frac{1}{3L_{\mathrm{s}}}\left[-u_{\mathrm{ab}} + u_{\mathrm{bc}} - 3(R_{\mathrm{s}} - R_{\mathrm{ext}})i_{\mathrm{b}} + 3\lambda p\dot{\theta}_{\mathrm{r}}(\phi_{\mathrm{a}} - 2\phi_{\mathrm{b}} + \phi_{\mathrm{c}})\right] \\
\dot{i}_{\mathrm{c}} &= -(\dot{i}_{\mathrm{a}} + \dot{i}_{\mathrm{b}})
\end{aligned} \tag{3}$$

where L_{s} is the motor inductance, u_{ab} and u_{bc} are the supply voltages (phase to phase), R_{s} is the motor resistance, R_{ext} is the external resistance responsible for regenerative braking of the BLDC motor, and θ_{r} is the rotor angular position.

3. Active Vibration Control with Regenerative Braking

The control strategy considered in this paper is based on field-oriented control (FOC), which enables efficient torque control of the BLDC motor in motoring mode and supports switching to the regenerative braking mode when the demanded control force is opposite to the relative velocity of the suspension mechanism. A block diagram of the proposed control system with the energy recovery braking subsystem is presented in Figure 2.

The FOC method requires decomposition of the three-phase instantaneous motor currents i_{a}, i_{b}, i_{c} into two current components i_{d}, i_{q} oriented in the rotating reference frame (*dq* frame) by using the Park transformation [26]:

$$\begin{bmatrix} i_{\mathrm{d}} \\ i_{\mathrm{q}} \end{bmatrix} = \frac{2}{3}\begin{bmatrix} \sin(p\theta_{\mathrm{r}}) & \sin(p\theta_{\mathrm{r}} - \frac{2}{3}\pi) & \sin(p\theta_{\mathrm{r}} + \frac{2}{3}\pi) \\ \cos(p\theta_{\mathrm{r}}) & \cos(p\theta_{\mathrm{r}} - \frac{2}{3}\pi) & \cos(p\theta_{\mathrm{r}} + \frac{2}{3}\pi) \end{bmatrix}\begin{bmatrix} i_{\mathrm{a}} \\ i_{\mathrm{b}} \\ i_{\mathrm{c}} \end{bmatrix} \tag{4}$$

where i_{d} and i_{q} are the resulting direct and quadrature components of the invariable current vector, respectively. Then, two proportional-integral controllers (PI in Figure 2) may be simply implemented to regulate the motor dynamics according to the following principles:

- Changing the direct component i_{d} is responsible for setting the magnetic flux.
- Adjusting the quadrature component i_{q} is responsible for controlling the motor torque.

https://doi.org/10.3390/en19153628

Typically, the direct component i_d of the current vector is settled to be zero ($i_d = 0$) in order to maximize the motor torque. Thus, the desired active force $(F_{ax})_{des}$ is assumed to be proportional to the setting current $(i_q)_{set}$ of the quadrature component:

$$(i_q)_{set} = \frac{r_e}{k_e}\underbrace{[-k_1\dot{q}_x - k_2(q_x - q_{sx})]}_{(F_{ax})_{des}} \quad \text{for} \quad (F_{ax})_{des} \cdot (\dot{q}_x - \dot{q}_{sx}) \geq 0 \quad \leftarrow \quad \text{motoring mode} \tag{5}$$

where k_e is the torque constant of BLDC motor, $\dot{q}_x$ is the absolute velocity of isolated body, $q_x - q_{sx}$ is the relative displacement of suspension system, and k_1 and k_2 are the control parameters responsible for reducing the harmful vibration (feedback gain k_1) or limiting the suspension stroke (feedback gain k_2) in the motoring mode of an electric actuator.

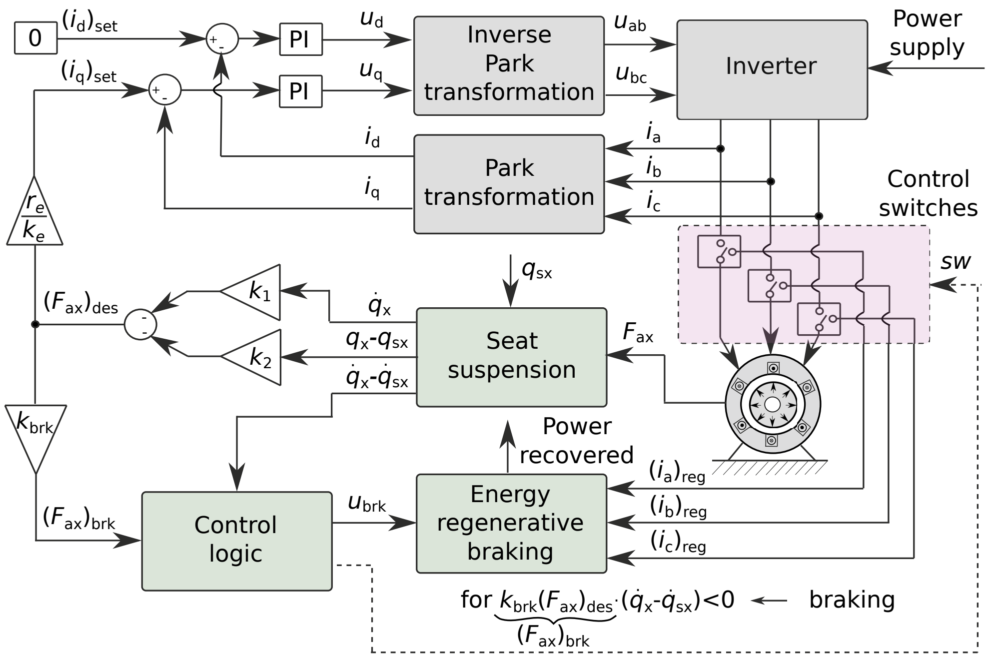

Figure 2. Block diagram of the proposed control system of an active horizontal seat suspension with the energy recovery braking subsystem.

When the setting currents $(i_d)_{set}$ and $(i_q)_{set}$ are specified, then the PI controllers should efficiently minimize the errors between demanded and actually measured motor currents by applying appropriate voltages u_d and u_q. In succession, these voltages specified in rotating reference frame (*dq* frame) shall be transformed back into stationary reference frame (*abc* frame) by employing the inverse Park transformation [26]:

$$\begin{bmatrix} u_{ab} \\ u_{bc} \end{bmatrix} = \frac{2}{3}\begin{bmatrix} \sqrt{3}\cos(p\theta_r - \frac{\pi}{3}) & -\sqrt{3}\sin(p\theta_r - \frac{\pi}{3}) \\ -\sqrt{3}\cos(p\theta_r) & \sqrt{3}\sin(p\theta_r) \end{bmatrix}\begin{bmatrix} u_d \\ u_q \end{bmatrix} \tag{6}$$

The braking force $(F_{ax})_{brk}$ generated by the BLDC motor during regenerative braking is approximated as a quadratic polynomial function with interactions between the relative velocity $\dot{q}_x - \dot{q}_{sx}$ of a suspension system and the voltage signal u_{brk} that is used for motor control in regenerative braking mode:

$$(F_{ax})_{brk} = a + b(\dot{q}_x - \dot{q}_{sx}) + c(\dot{q}_x - \dot{q}_{sx})^2 + du_{brk} + e(\dot{q}_x - \dot{q}_{sx})u_{brk} \tag{7}$$

where a, b, c, d and e are the numerical constants to be calculated by using the least square method from the measurement results. The inverse polynomial model defining the control signal of the BLDC motor in braking mode is as follows:

$$u_{\mathrm{brk}} = \frac{-a-b(\dot{q}_{\mathrm{x}}-\dot{q}_{\mathrm{sx}})-c(\dot{q}_{\mathrm{x}}-\dot{q}_{\mathrm{sx}})^2+(F_{\mathrm{ax}})_{\mathrm{brk}}}{d+e(\dot{q}_{\mathrm{x}}-\dot{q}_{\mathrm{sx}})} \quad \text{for} \quad \underbrace{k_{\mathrm{brk}}(F_{\mathrm{ax}})_{\mathrm{des}}}_{(F_{\mathrm{ax}})_{\mathrm{brk}}} \cdot (\dot{q}_{\mathrm{x}}-\dot{q}_{\mathrm{sx}}) < 0 \quad \leftarrow \quad \text{braking mode} \tag{8}$$

where k_{brk} is the ratio between the braking force $(F_{\mathrm{ax}})_{\mathrm{brk}}$ achieved for an original hardware implementation of the energy recovery braking subsystem and the desired active force $(F_{\mathrm{ax}})_{\mathrm{des}}$ of a specific motor type. The numerical parameters of the BLDC motor and its braking subsystem are listed in Appendix A.

4. Hardware Implementation

In this work, a system was developed to implement the regenerative braking function for a BLDC motor. Braking resistors (R_{1a}, R_{1b}, R_{1c}, …, R_{5a}, R_{5b}, R_{5c}) are connected to the three windings of the motor using switching transistors (T_{1a}, T_{1b}, T_{1c}, …, T_{5a}, T_{5b}, T_{5c}). The schematic diagram of this solution is presented in Figure 3.

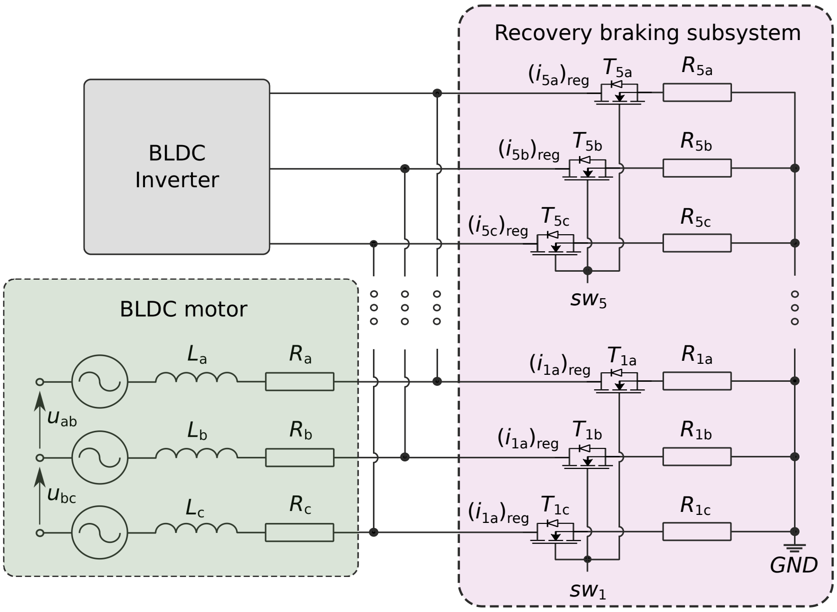

Figure 3. Hardware implementation of the energy recovery braking subsystem operating together with BLDC motor.

An external microcontroller converts the analogue braking voltage signal u_{brk} generated by the control logic into one of five digital signals (sw_1, …, sw_5). Each of these signals activates a specific group of MOSFET transistors via a transistor driver. At any given time, only one subgroup of transistors can be activated, enabling the braking intensity to be divided into five levels, ranging from minimum to maximum. The resistance values of individual resistors are determined experimentally to ensure an even distribution of braking force levels. The highest braking intensity corresponds to $u_{\mathrm{brk}} = 5$ V, while the lowest corresponds to $u_{\mathrm{brk}} = 0$ V. The corresponding resistance levels are as follows: 0.1 Ω; 0.15 Ω; 0.22 Ω, 0.33 Ω and 0.47 Ω. The currents $(i_{1a})_{\mathrm{reg}}$, $(i_{1b})_{\mathrm{reg}}$, $(i_{1c})_{\mathrm{reg}}$, …, $(i_{5a})_{\mathrm{reg}}$, $(i_{5b})_{\mathrm{reg}}$, $(i_{5c})_{\mathrm{reg}}$ induced in the motor windings during regenerative braking are measured using current sensors (ACS742 manufactured by Allegro Microsystems) based on the Hall effect. This approach enables precise recording and further analysis of the regenerated current intensity.

In the present laboratory prototype, the electrical energy generated during regenerative braking was not stored in a battery or supercapacitor. Instead, it was dissipated in a controlled resistor network connected to the BLDC motor windings through MOSFET switches. Therefore, the reported current and power values should be interpreted as the recoverable electrical power available in the braking branch, rather than as net stored energy. The purpose of this implementation was to quantify the energy recovery potential of the suspension system and to verify the controllability of the regenerative braking force. The RMS current in the braking branch is calculated as

$$I_{\mathrm{RMS}} = \sqrt{\frac{1}{T}\int_0^T i^2(t)\,dt}, \tag{9}$$

or, for sampled data, as

$$I_{\mathrm{RMS}} = \sqrt{\frac{1}{N}\sum_{n=1}^{N} i^2[n]}. \tag{10}$$

For the resistor network used in the regenerative braking branch, the instantaneous electrical power is determined from the measured phase currents and active resistance level as

$$P_{\mathrm{brk}}(t) = \sum_j R_j i_j^2(t), \tag{11}$$

where R_j is the resistance connected in the active braking branch and $i_j(t)$ is the corresponding measured current. The average electrical power and recoverable energy over the measurement interval T are then defined as

$$P_{\mathrm{avg}} = \frac{1}{T}\int_0^T P_{\mathrm{brk}}(t)\,dt, \tag{12}$$

$$E_{\mathrm{brk}} = \int_0^T P_{\mathrm{brk}}(t)\,dt. \tag{13}$$

If the power consumed by the drive in motoring mode is measured in future experiments, the net energy balance can be evaluated as

$$E_{\mathrm{net}} = E_{\mathrm{mot}} - E_{\mathrm{brk}}, \tag{14}$$

and the corresponding recovery ratio can be estimated as

$$\eta_{\mathrm{rec}} = \frac{E_{\mathrm{brk}}}{E_{\mathrm{mot}}} \cdot 100\%. \tag{15}$$

In the present study, the net energy balance of the complete drive system was not evaluated because the prototype did not include a bidirectional DC-link converter or energy storage unit. Losses in the inverter, switching elements and motor windings were therefore not separated from the braking-branch measurement and should be addressed in future work.

5. System Identification

The next objective of the research is to analyze how the active braking force generated by the BLDC motor changes as a function of the relative displacement and different set values of the quadrature current component $(i_{\mathrm{q}})_{\mathrm{set}}$. In Figure 4a, the experimental data (dotted lines-measurements) showing the actual active force exerted by the motor for different values of $(i_q)_{set}$, i.e., 0 A, 5 A, 10 A, 15 A, and 20 A, are presented. In this case, the sinusoidal movement of suspension mechanism is applied at relative displacement of ± 0.014 m. The solid lines (approximations) show a very close match to the measurements, indicating a reliable approximation model (Figure 4b). The force output of an electric motor increases proportionally in the current domain. This suggests that the active force in motoring mode is primarily a function of the setting current, whereas the relative displacement of the suspension mechanism is irrelevant. Therefore, the objective is to identify the control signal (i.e., current) that corresponds to a desired active force.

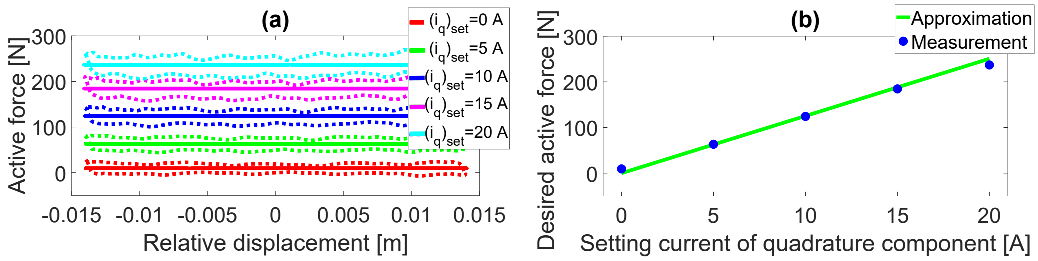

Figure 4. Measured active forces (dots) and their average values (solid lines) in motoring mode versus the relative displacement of the suspension mechanism for different quadrature current settings (**a**) and linear approximation of the desired active force (**b**).

The identification process shown in Figure 5 provides a model of the BLDC motor operating in regenerative braking mode, with forward and inverse mappings between braking force, braking control signal, and relative suspension velocity. Experimental measurements are required to model the regenerated braking force as a function of brake signal and relative velocity. In the first step, the actual braking force is obtained for different combinations of control voltage and relative velocity. Figure 5a presents the braking force as a function of brake signal and relative velocity, where the blue points represent measured data. The colored surface represents the fitted quadratic regression model used to approximate the measured braking force. This surface shows that the braking force increases with the brake signal and changes with relative velocity. Figure 5b shows the inverse model of the control signal as a function of braking force and relative velocity. This inverse function is required for real-time control because it enables the controller to calculate the braking signal needed to obtain a desired braking force for a given relative velocity.

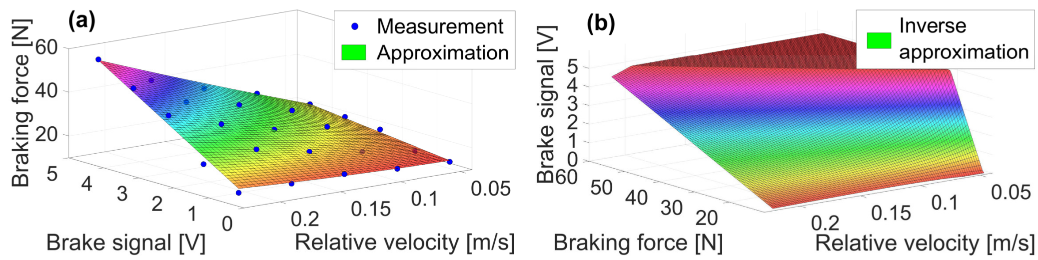

Figure 5. Measured and approximated braking force versus relative velocity and brake signal (**a**) and its inverse approximation (**b**).

6. Laboratory Experimental Results

6.1. Experimental Procedure and Signal Processing

Figure 6 displays the excitation signals employed throughout the experimental testing of the seat suspension system, comparing three distinct input scenarios across passive, active, and regenerative control modes. The visualization is structured with time-domain profiles on the left and corresponding frequency-domain responses on the right. In the time-domain plot (Figure 6a), the base acceleration over an exemplary 3 second duration to illustrate the transient behavior of each excitation signal. Figure 6b presents the Power Spectral Density (PSD) functions of these excitations. By measuring power per unit frequency, this graph demonstrates how energy is distributed across the spectrum, revealing the exact energy levels delivered at specific frequencies. The three curves, labeled WN1, WN2, and WN3, correspond to low, medium, and high vibration intensities, respectively. These signals function as band-limited white noise, produced by a random waveform generator, with their spectral characteristics established through low-pass and high-pass filtering within a 0.5–10 Hz frequency range. Although these signals do not originate from real-world on-road vehicle measurements, they are highly effective standard tools used in seat manufacturers' test laboratories to evaluate the vibration-isolation performance of seat suspension systems. This specific arrangement enables a highly controlled study of seat suspension dynamics, allowing researchers to adjust the motor's output and precisely observe how different vibration intensities impact the behavior of the suspension system when loaded by different masses. The time of a single measurement is 300 s and data from the acceleration and displacement sensors are recorded at a sampling rate of 1 ms.

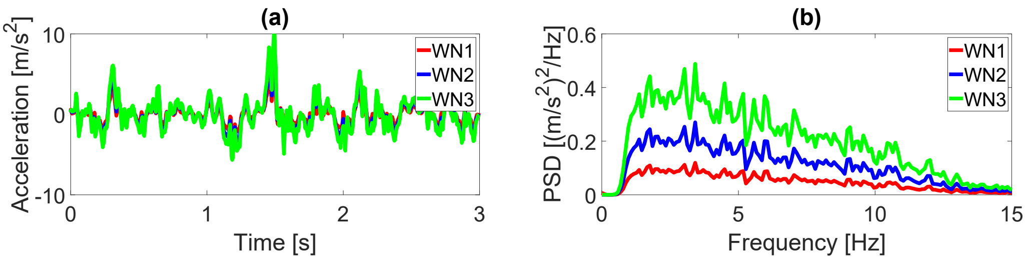

Figure 6. Time histories of the excitation signals (**a**) and their Power Spectral Densities (PSDs) (**b**) at different intensities: WN1, WN2 and WN3.

The seat displacement, base displacement or acceleration, and regenerated phase currents were recorded synchronously. The current in the regenerative braking branch was measured using ACS742 Hall-effect current sensors. Hall-effect linear current sensors with over-current fault output for <100 V isolation applications are utilized in order to continuously monitor the phase currents. The switching logic between motoring mode and regenerative braking mode is realized by the control algorithm defined by Equations (5) and (8). If the desired active force and the relative velocity of suspension system are consistent, then the motoring mode is turned on. In turn, if the signs of the desired force and the relative velocity are opposite, then the braking mode is activated. The switching delays between these modes are achieved at the level of the micro-controller sampling time, i.e., 1 ms. The transmissibility functions were calculated in the frequency domain as the ratio between the seat response and base excitation.

6.2. Dynamic Performance and Energy Recovery Evaluation

Figure 7 illustrates the time-domain behaviour of the BLDC motor and the regenerative braking subsystem for three excitation intensities,: WN1, WN2 and WN3. The subplots are arranged in pairs. In the left column, the setting current of the quadrature-axis component $(i_q)_{set}$ and the braking control voltage u_{brk} are shown. In the right column, the corresponding regenerated phase currents $(i_a)_{reg}$, $(i_b)_{reg}$ and $(i_c)_{reg}$ are presented. The shaded regions indicate intervals in which the regenerative braking branch is activated. During these intervals, the braking signal u_{brk} controls the connection of the resistor network to the motor windings, and the generated phase currents represent the electrical response of the BLDC motor in regenerative braking mode.

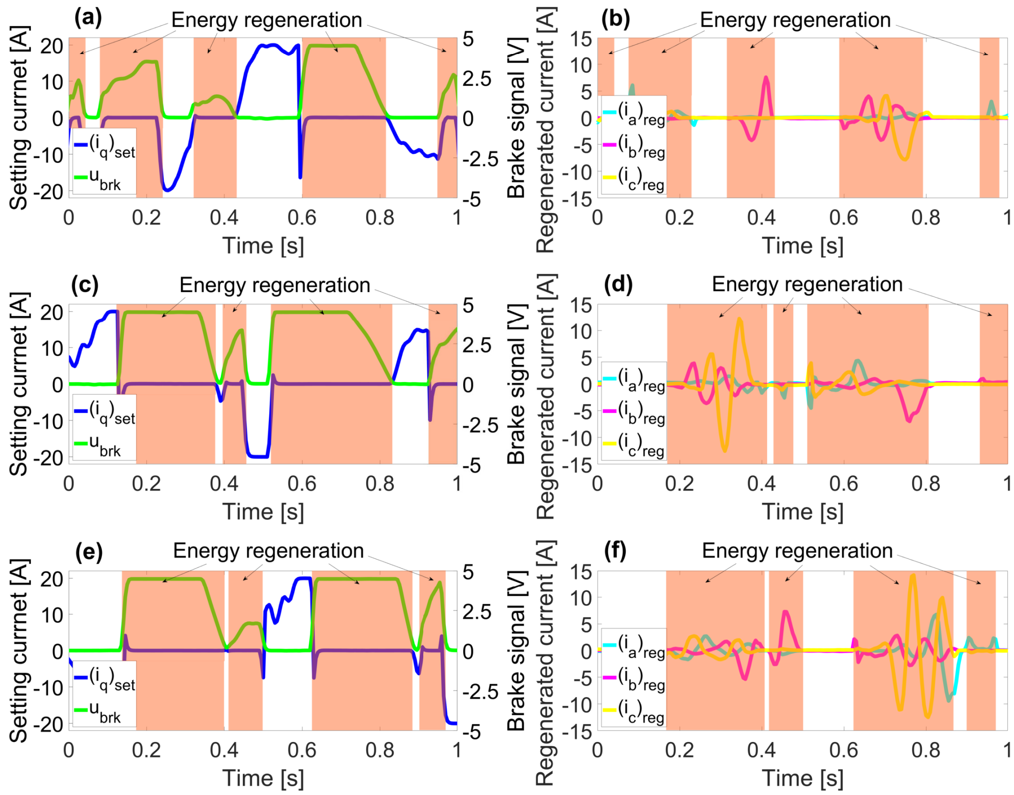

Figure 7. Time-domain signals of the BLDC motor and regenerative braking subsystem for different excitation intensities: WN1 (**a**,**b**), WN2 (**c**,**d**) and WN3 (**e**,**f**). The left column shows $(i_q)_{set}$ and u_{brk}, while the right column shows regenerated phase currents $(i_a)_{reg}$, $(i_b)_{reg}$ and $(i_c)_{reg}$. Shaded regions indicate regenerative braking intervals.

The time-domain results show that the activation of the braking signal u_{brk} corresponds to the intervals in which the BLDC motor works as a generator and the resistor network dissipates the generated electrical power. In the shaded regions, $(i_q)_{set}$ is reduced or changes according to the switching condition, while u_{brk} determines the braking intensity. As the excitation intensity increases from WN1 to WN3, the relative velocity of the suspension mechanism increases, which produces higher induced electromotive force in the motor windings. Consequently, the regenerated phase currents have larger amplitudes and the recoverable electrical power increases. This confirms the expected physical relationship between mechanical vibration intensity, regenerative braking current and recoverable electrical power.

The results in Figure 8 illustrate the transmissibility functions of different seat suspension systems (passive, active and regenerative) under varying load conditions (40 kg, 60 kg and 80 kg) and different excitation intensities (WN1–WN3). In the case of passive suspension system (Figure 8a,b) the effect of excitation intensity (Figure 8a,c,e –left panel) in the fact that the transmissibility is highest at low frequencies (0–3 Hz), gradually decreasing at higher frequencies. Variations between WN1–WN3 are minor but indicate that higher excitation intensities very slightly increase transmissibility at certain frequencies. The effect of mass load (Figure 8b,d,f–right panel) shows that increasing the mass load from 40 kg to 80 kg results in a slight shift in peak transmissibility. The transmissibility at lower frequencies (approx. 0.5 Hz) is firstly higher for lower mass loads (40 kg), but then reduces (in range 1–2 Hz) as mass increases, suggesting improved damping with heavier mass loads. Above 2 Hz to the end of the tested frequency range, the effect is the opposite.

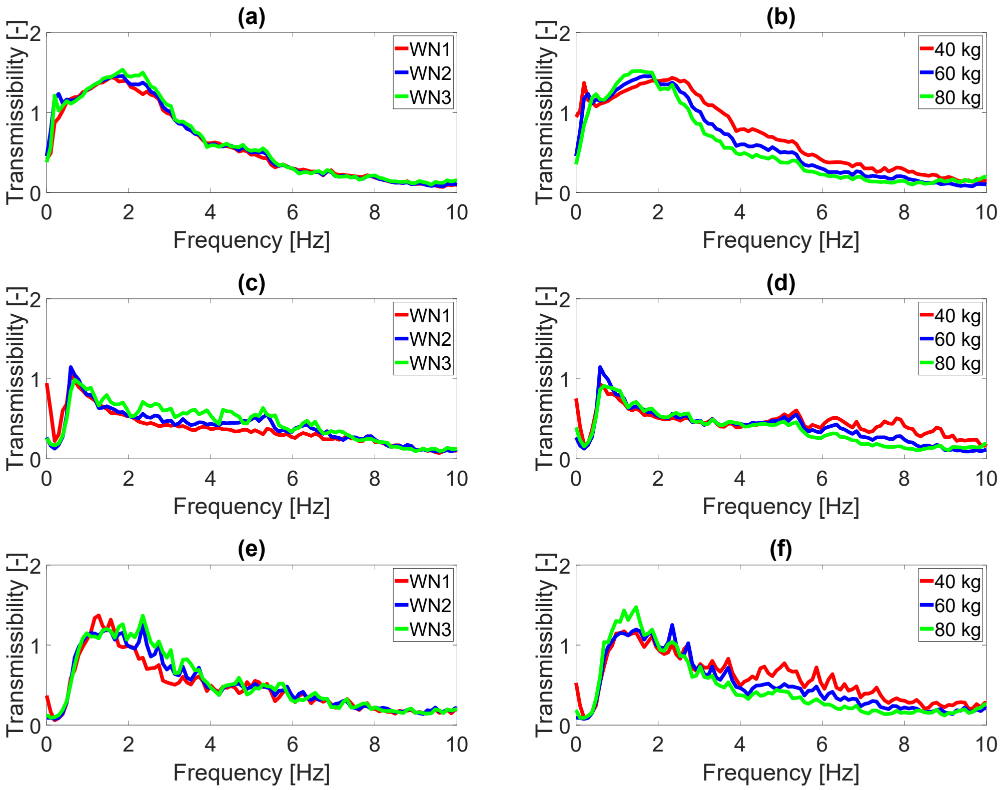

Figure 8. Transmissibility functions of the passive (**a**), active (**c**) and regenerative (**e**) seat suspension system at different excitation intensity: WN1–WN3 and the same mass load: 60 kg (figures on the left hand side); transmissibility functions of the passive (**b**), active (**d**), and regenerative (**f**) seat suspension system at various mass load: 40–80 kg, the same excitation intensity WN2.

Figure 8c,d shows the results for the fully active suspension system. Compared with the passive suspension, the active system substantially reduces the transmissibility over the analyzed frequency range. The transmissibility remains relatively stable across the excitation signals WN1–WN3 and is mostly below unity, which confirms improved vibration isolation. The influence of mass loading is visible mainly around the low-frequency peak and at higher frequencies, where the increased inertial load modifies the dynamic response of the seat suspension.

Figure 8e,f present the vibro-isolation properties of the proposed regenerative suspension system. The regenerative mode reduces transmissibility compared with the passive system; however, its vibration attenuation is lower than that of the fully active system, especially in the low-frequency range of approximately 1–3 Hz. This behaviour reflects the fundamental trade-off between vibration reduction and energy recovery. In the regenerative mode, a part of the mechanical vibration energy is converted into electrical energy and dissipated in the braking resistor network. As a result, the system provides additional damping and measurable recoverable electrical power, but it does not reproduce the full control authority of the active mode. The numerical values of SEAT factor and suspension travel for the passive, active and regenerative seat suspension at different excitation intensities and mass loads are reported in Table 1.

The SEAT factor was calculated as the ratio between the RMS acceleration of the seat and the RMS acceleration of the suspension base:

$$SEAT = \frac{a_{\text{seat,RMS}}}{a_{\text{base,RMS}}}, \tag{16}$$

where

$$a_{\text{seat,RMS}} = \sqrt{\frac{1}{T}\int_0^T a_{\text{seat}}^2(t)\,dt}, \tag{17}$$

$$a_{\text{base,RMS}} = \sqrt{\frac{1}{T}\int_0^T a_{\text{base}}^2(t)\,dt}. \tag{18}$$

The percentage reduction in SEAT factor relative to the passive suspension was evaluated as

$$\Delta SEAT = \frac{SEAT_{\text{passive}} - SEAT_{\text{mode}}}{SEAT_{\text{passive}}} \cdot 100\%, \tag{19}$$

where $SEAT_{\text{mode}}$ denotes either the active or regenerative mode. The relative change in suspension travel was calculated as

$$\Delta s = \frac{s_{\text{mode}} - s_{\text{passive}}}{s_{\text{passive}}} \cdot 100\%. \tag{20}$$

Based on Table 1, the fully active suspension reduced the SEAT factor by approximately 43–57% compared with the passive suspension. The regenerative suspension reduced the SEAT factor by approximately 17–25% relative to the passive case. At the same time, both active and regenerative modes generally increased suspension travel in comparison with the passive suspension. Therefore, the results indicate a clear trade-off: the active mode provides the strongest vibration attenuation, whereas the regenerative mode provides moderate vibration attenuation while generating electrical power in the braking branch.

Table 1. Numerical values of the SEAT factor and suspension travel for the passive, active and regenerative seat suspension at different excitation intensity and various mass load.

	Mass Load					
	Passive		**Active**		**Regenerative**	
Excitation signal	SEAT factor	Suspension travel	SEAT factor	Suspension travel	SEAT factor	Suspension travel
Mass load 40 kg						
WN1	1.172	22.5 mm	0.501	35.8 mm	0.886	36.3 mm
WN2	1.178	29.5 mm	0.536	39.1 mm	0.885	33.2 mm
WN3	1.186	34.3 mm	0.609	39.1 mm	0.936	40.1 mm
Mass load 60 kg						
WN1	1.123	26.3 mm	0.507	35.9 mm	0.845	36.9 mm
WN2	1.145	34.3 mm	0.551	40.5 mm	0.894	38.5 mm
WN3	1.186	38.4 mm	0.637	40.2 mm	0.953	41.0 mm
Mass load 80 kg						
WN1	1.095	30.0 mm	0.501	37.6 mm	0.832	35.5 mm
WN2	1.132	37.1 mm	0.563	40.8 mm	0.927	39.3 mm
WN3	1.179	40.5 mm	0.669	40.7 mm	0.975	41.5 mm

Figure 9 presents the RMS current and electrical power generated in the regenerative braking branch under different excitation signals and mass loads. The RMS current increases with excitation intensity from WN1 to WN3 and also generally increases with mass load. The highest RMS current, 2.654 A, occurs for WN3 and the 80 kg load, whereas the lowest value, 1.02 A, occurs for WN1 and the 40 kg load. The electrical power follows the same trend. The highest value, 7.692 W, is observed for WN3 and the 80 kg load, while the lowest value, 2.13 W, is observed for WN1 and the 40 kg load. These results confirm that stronger excitation and heavier loads increase the mechanical energy available for conversion during regenerative braking. In the present prototype, this power was dissipated in the braking resistor network; therefore, it should be interpreted as recoverable electrical power rather than net stored energy.

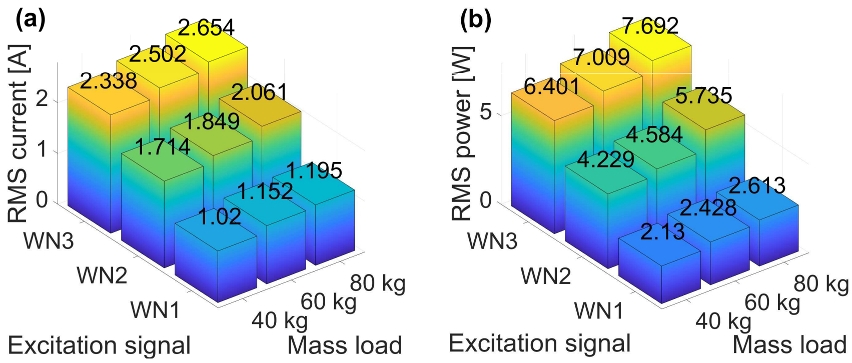

Figure 9. RMS current (**a**) and electrical power (**b**) generated in the regenerative braking branch at different excitation intensities WN1–WN3 and mass loads of 40–80 kg.

7. Discussion

7.1. Trade-Off Between Vibration Attenuation and Recoverable Electrical Power

The results demonstrate that the fully active suspension provides the best vibration isolation, whereas the regenerative mode provides a compromise between vibration reduction and recoverable electrical power. In active mode, the BLDC motor uses external electrical energy to generate the demanded control force. In regenerative mode, the motor produces a braking force only when the force direction and relative velocity satisfy the regenerative condition. Consequently, the regenerative mode has lower control authority than the active mode, but it reduces the external energy demand by generating electrical power in the braking branch.

The quantitative values in Table 1 confirm this behaviour. The active mode reduced the SEAT factor by approximately 43–57% relative to the passive suspension, whereas the regenerative mode reduced it by approximately 17–25%. However, the active and regenerative modes often increased suspension travel compared with the passive case. This means that comfort improvement should be evaluated together with stroke limitation. In practical applications, the controller parameters should therefore not only be tuned to minimize vibration transmitted to the occupant, but also to maintain acceptable suspension travel and maximize the recoverable electrical power.

7.2. Implications for Human Exposure and Ride Comfort

Since the investigated system is intended for seat suspension applications, the transmissibility results should also be interpreted from the perspective of human exposure to horizontal whole-body vibration [27]. The 40–80 kg inertial loads used in this study represent simplified occupant mass conditions; therefore, the results should be treated as mechanical indicators of potential ride comfort rather than direct human-subject measurements. The frequency-dependent transmissibility curves show that the suspension configuration influences the vibration transmitted to the seated body, particularly in the low-frequency range where ride comfort and body resonance effects are important. In future work, the assessment should be extended using ISO 2631-1-based frequency-weighted acceleration analysis [28] and, if possible, anthropodynamic seat–occupant models. Such an extension would allow for the vibration isolation and energy recovery performance to be linked directly with occupant comfort and ergonomics.

https://doi.org/10.3390/en19153628

7.3. Limitations of the Present Prototype

The main limitation of the present prototype is that the generated electrical energy was dissipated in braking resistors and was not stored in an energy storage device. As a result, the reported electrical power quantifies the recoverable energy potential of the system rather than the net amount of energy stored or reused. A second limitation is that losses in the inverter, motor windings and switching devices were not separately identified. Future work should include a bidirectional DC-link converter, a supercapacitor or battery storage unit, and direct measurement of both motoring energy consumption and regenerative energy flow.

8. Conclusions

The experimental results confirm that the fully active suspension provides the highest vibration isolation performance, reducing the SEAT factor by approximately 43–57% compared with the passive suspension. The regenerative mode provides a lower, but still significant, reduction of the SEAT factor, approximately 17–25% relative to the passive case, while simultaneously generating measurable electrical power in the braking branch. The maximum measured electrical power was 7.692 W for the WN3 excitation and the 80 kg load. These results demonstrate that regenerative braking can not only be used for additional damping, but also for partial recovery of vibration energy in horizontal seat suspension systems. The identification results show that both active and regenerative braking forces of the BLDC motor can be represented using simple approximation models suitable for real-time implementation. However, the regenerative mode should be interpreted as a compromise between vibration attenuation and recoverable electrical power because it does not provide the same control authority as the fully active mode. The present prototype did not include an energy storage unit; therefore, the reported power values represent recoverable power dissipated in the braking resistor network rather than net stored energy. Future work should include a bidirectional power converter, DC-link energy storage, loss analysis and ISO 2631-1-based ride comfort assessment.

Author Contributions: Conceptualization, I.M. and A.B.; methodology, T.K. (Tomasz Krzyzynski); software, T.K. (Tomasz Krolikowski), S.P. and B.J.; validation, I.M. and B.J.; formal analysis, I.M., T.K. (Tomasz Krolikowski) and A.B.; investigation, I.M. and S.P.; resources, T.K. (Tomasz Krolikowski), T.K. (Tomasz Krzyzynski) and B.J.; data curation, I.M. and S.P.; writing—original draft preparation, I.M., A.B. and S.P.; writing—review and editing, I.M., A.B. and S.P.; visualization, I.M. and B.J.; supervision, T.K. (Tomasz Krolikowski), T.K. (Tomasz Krzyzynski); project administration, T.K. (Tomasz Krolikowski), T.K. (Tomasz Krzyzynski); funding acquisition, T.K. (Tomasz Krolikowski), T.K. (Tomasz Krzyzynski) and B.J. All authors have read and agreed to the published version of the manuscript.

Funding: This research received no external funding.

Data Availability Statement: The raw and processed experimental data, including vibration signals, transmissibility functions, SEAT factors, suspension travel values, regenerated current and electrical power values, are available from the corresponding author upon reasonable request.

Conflicts of Interest: The authors declare no conflicts of interest.

Abbreviations

The following abbreviations are used in this manuscript:

BLDC	Brushless direct current
FOC	Field-oriented control
IoT	Internet of Things

MOSFET	Metal–oxide–semiconductor field-effect transistor
PMSM	Permanent magnet synchronous motor
RMS	Root mean square
SEAT	Seat effective amplitude transmissibility

Appendix A. Numerical Parameters of the BLDC Motor and Its Braking Subsystem

Table A1. Model parameters and control gains adopted for the simulation study.

Model Parameters	Numerical Values
amplitude of a flux induced by permanent magnets (λ)	0.00733 Vs
first controller setting (k_1)	7 Ns/m
second controller setting (k_2)	20 N/m
ratio between maximum braking force and maximum active force (k_{brk})	0.2
torque constant of a motor (k_e)	0.044 Nm/A
inductance of a motor (L_s)	$0.1 \cdot 10^{-3}$ H
length of the lever arm (r_e)	0.045 m
number of pole pairs (p)	3
resistance of a motor (R_s)	0.0675 Ω

References

1. Hao, J.; Li, W.; Zhai, J.; Chen, H. Progress in high-strain perovskite piezoelectric ceramics. *Mater. Sci. Eng. R Rep.* **2019**, *135*, 1–57. [CrossRef]
2. Ponraj, B.; Bhimireddi, R.; Varma, K.B.R. Effect of nano- and micron-sized K0.5Na0.5NbO3 fillers on the dielectric and piezoelectric properties of PVDF composites. *J. Adv. Ceram.* **2016**, *5*, 308–320. [CrossRef]
3. Lang, S.B.; Muensit, S.; Lang S, Muensit, S. Review of some lesser-known applications of piezoelectric and pyroelectric polymers. *Appl. Phys. A* **2006**, *85*, 125–134. [CrossRef]
4. Zhu, J.; Jia, L.; Huang, R. Electrospinning poly(l-lactic acid) piezoelectric ordered porous nanofibers for strain sensing and energy harvesting. *J. Mater. Sci. Mater. Electron.* **2017**, *28*, 12080–12085. [CrossRef]
5. Hou, C.; Li, Z.; Fei, C.; Lin, Q.; Luo, X.; Wei, X.; Yang, Y.; Lu, Q.; Quan, Y.; Dong, G.; et al. Gradient piezoelectric composites for ultrasonic transducer design and imaging applications. *J. Mater.* **2025**, *11*, 101049. [CrossRef]
6. Kapat, K.; Shubhra, Q.T.H.; Zhou, M.; Leeuwenburgh, S. Piezoelectric Nano-Biomaterials for Biomedicine and Tissue Regeneration. *Adv. Funct. Mater.* **2020**, *30*, 1909045. [CrossRef]
7. Song, Y.; Yang, C.H.; Hong, S.K.; Hwang, S.J.; Kim, J.H.; Choi, J.Y.; Ryu, S.K.; Sung, T.H. Road energy harvester designed as a macro-power source using the piezoelectric effect. *Int. J. Hydrogen Energy* **2016**, *41*, 12563–12568. [CrossRef]
8. Gao, M.Y.; Wang, P.; Cao, Y.; Chen, R.; Liu, C. A rail-borne piezoelectric transducer for energy harvesting of railway vibration. *J. Vibroengineering* **2016**, *18*, 4647–4663. [CrossRef]
9. Wang, H.; Jasim, A.; Chen, X. Energy harvesting technologies in roadway and bridge for different applications—A comprehensive review. *Appl. Energy* **2018**, *212*, 1083–1094. [CrossRef]
10. Chen, N.; Jung, H.J.; Jabbar, H.; Sung, T.H.; Wei, T. A piezoelectric impact-induced vibration cantilever energy harvester from speed bump with a low-power power management circuit. *Sens. Actuators A Phys.* **2017**, *254*, 134–144. [CrossRef]
11. Lee, P.J.; Jain, S.K.; Bhonsale, A.; Voigt, A.H.; Dh, e M.; Kancharla, K.; Singla, V.; Naniwadekar, A.; Estes, N.A.M.; Saba, S.F.; et al. Early experience with intracardiac echocardiography guidance for atrial leadless pacemaker implantation. *Heart Rhythm* 2025, *in press*. [CrossRef] [PubMed]
12. Ahmed, S.; Kakkar, V. An Electret-Based Angular Electrostatic Energy Harvester for Battery-Less Cardiac and Neural Implants. *IEEE Access* **2017**, *5*, 19631–19643. [CrossRef]
13. Linh, V.T.N.; Han, S.; Koh, E.; Kim, S.; Jung, H.S.; Koo, J. Advances in wearable electronics for monitoring human organs: Bridging external and internal health assessments. *Biomaterials* **2025**, *314*, 122865. [CrossRef] [PubMed]
14. Bai, S.; Liu, C. Overview of energy harvesting and emission reduction technologies in hybrid electric vehicles. *Renew. Sustain. Energy Rev.* **2021**, *147*, 111188. [CrossRef]
15. Bentouba, S.; Zioui, N.; Breuhaus, P.; Bourouis, M. Overview of the Potential of Energy Harvesting Sources in Electric Vehicles. *Energies* **2023**, *16*, 5193. [CrossRef]

16. Hadas, Z.; Rubes, O.; Ksica, F.; Chalupa, J. Kinetic Electromagnetic Energy Harvester for Railway Applications—Development and Test with Wireless Sensor. *Sensors* **2022**, *22*, 905. [CrossRef] [PubMed]
17. Taithongchai, T.; Leelarasmee, E. Adaptive electromagnetic energy harvesting circuit for wireless sensor application. In *Proceedings of the 6th International Conference on Electrical Engineering/Electronics, Computer, Telecommunications and Information Technology*; IEEE: Piscataway, NJ, USA, 2009; pp. 278–281. [CrossRef]
18. Li, Z.; Yan, Z.; Luo, J.; Yang, Z. Performance comparison of electromagnetic energy harvesters based on magnet arrays of alternating polarity and configuration. *Energy Convers. Manag.* **2019**, *179*, 132–140. [CrossRef]
19. Halim, M.A.; Park, J.Y. Modeling and experiment of a handy motion driven, frequency up-converting electromagnetic energy harvester using transverse impact by spherical ball. *Sens. Actuators A Phys.* **2015**, *229*, 50–58. [CrossRef]
20. Qiu, J.; Liu, X.; Hu, Z.; Chang, Q.; Gao, Y.; Yang, J.; Wen, J.; Tang, X.; Hu, W. Multi-directional electromagnetic vibration energy harvester using circular Halbach array. *AIP Adv.* **2017**, *7*, 056672. [CrossRef]
21. Sun, S.; Dai, X.; Wang, K.; Xiang, X.; Ding, G.; Zhao, X. Nonlinear Electromagnetic Vibration Energy Harvester With Closed Magnetic Circuit. *IEEE Magn. Lett.* **2018**, *9*, 6102604. [CrossRef]
22. Yang, Y.; Liu, C.; Chen, L.; Zhang, X. Phase deviation of semi-active suspension control and its compensation with inertial suspension. *Acta Mech. Sin.* **2024**, *40*, 523367. [CrossRef]
23. Qin, A.; Zhang, B.; Ning, D.; Tan, B.; Du, H. A self-sensing approach for estimating suspension displacement and velocity in semi-active electromagnetic dampers. *Mech. Syst. Signal Process.* **2024**, *208*, 111049. [CrossRef]
24. Krzyzynski, T.; Maciejewski, I.; Meyer, L.; Meyer, H. *Modelling and Control Design of Vibration Reduction Systems*; Springer Nature: Cham, Switzerland, 2019. [CrossRef]
25. Krause, P.C.; Wasynczuk, O.; Sudhoff, S.D.; Pekarek, S. *Analysis of Electric Machinery and Drive Systems*; John Willey & Sons: Hoboken, NJ, USA, 2013. [CrossRef]
26. Chattopadhyay, S.; Mitra, M.; Sengupta, S. *Electric Power Quality: Clarke and Park Transform*; Springer Science & Business Media: Dordrecht, The Netherlands, 2011. [CrossRef]
27. Karpenko, M.; Prentkovskis, O.; Skačkauskas, P. Analysing the impact of electric kick-scooters on drivers: Vibration and frequency transmission during the ride on different types of urban pavements. *Eksploat. Niezawodn.–Maint. Reliab.* **2025**, *27*, 199893. [CrossRef]
28. *ISO 2631-1:1997*; Mechanical Vibration and Shock—Evaluation of Human Exposure to Whole-Body Vibration—Part 1: General Requirements. International Organization for Standardization (ISO): Geneva, Switzerland, 1997.